NeuroImage 198 (2019) 160–169

Contents lists available at ScienceDirect

NeuroImage

journal homepage: www.elsevier.com/locate/neuroimage

Noninvasive noncontact speckle contrast diffuse correlation tomography of cerebral blood flow in rats

Chong Huang [a], Siavash Mazdeyasna [a], Li Chen [b], Elie G. Abu Jawdeh [c], Henrietta S. Bada [c], Kathryn E. Saatman [d], Lei Chen [d,*], Guoqiang Yu [a,**]

[a] Department of Biomedical Engineering, University of Kentucky, Lexington, KY, 40506, USA
[b] Department of Biostatistics, College of Public Health. University of Kentucky, Lexington, KY, 40536, USA
[c] Department of Pediatrics, College of Medicine, University of Kentucky, Lexington, KY, 40536, USA
[d] Department of Physiology, Spinal Cord and Brain Injury Research Center, University of Kentucky, Lexington, KY, 40536, USA

ARTICLE INFO

Keywords:
Cerebral blood flow
Speckle contrast diffuse correlation tomography
Noninvasive
Noncontact
3D imaging
Near-infrared light

ABSTRACT

Continuous and longitudinal imaging of cerebral blood flow (CBF) variations provide vital information to investigate pathophysiology and interventions for a variety of neurological and cerebral diseases. An innovative noncontact speckle contrast diffuse correlation tomography (scDCT) system was downscaled and adapted for noninvasive imaging of CBF distributions in rat brain through intact scalp and skull. Algorithms for 2D mapping and 3D image reconstruction of CBF distributions were developed and optimized. The continuous imaging capability of the system was shown by imaging global CBF increases during CO_2 inhalations and regional CBF decreases across two hemispheres during sequential unilateral and bilateral common carotid artery ligations. The longitudinal imaging capability was demonstrated by imaging CBF variations over a long recovery period of 14 days after an acute stroke. Compared to the 2D mapping method, the 3D imaging method reduces partial volume effects, but needs more computation time for image reconstruction. Results from this study generally agree with those reported in the literature using similar protocols to induce CBF changes in rats. The scDCT enables a relatively large penetration depth (up to ~10 mm), which is sufficient for transcranial brain measurements in small animals and human neonates. Ultimately, we expect to provide a noninvasive noncontact cerebral imager for basic neuroscience research in small animal models and clinical applications in human neonates.

1. Introduction

Cerebral blood flow (CBF) is tightly coupled with neural activities and instantly regulated to meet brain metabolic demands. Cerebral hyper-perfusion (excessive CBF) can raise intracranial pressure or induce headache or hemorrhage, while cerebral hypo-perfusion (insufficient CBF) can lead to depression of cortical function or ischemic injury. Therefore, continuous and longitudinal monitoring of CBF variations is crucial for understanding pathological mechanisms and developing medical interventions for a variety of neurological and cerebral diseases. Small rodents (mice and rats) have been the leading model organisms used in preclinical neuroscience research (Chesselet and Carmichael, 2012; Durukan et al., 2008; Ellenbroek and Youn, 2016; Schaller and Graf, 2002; Stagliano et al., 1999). Since their introduction to the laboratory more than one century ago, rodents still make up 95% of the animal models used in biomedical research today. Mice have a more prominent role compared to rats due to the availability of a much larger genetic toolbox, while rats are closer to humans (especially neonates) compared to mice.

Technologies capable of imaging CBF in both animals and humans are critically needed for translational studies of cerebral diseases, which are often associated with regional cerebral ischemia and hypoxia. In contrast to large imaging modalities such as computer tomography (CT), magnetic resonance imaging (MRI) and positron emission tomography (PET), optical instruments are fast, continuous, inexpensive, and portable (Boas et al., 2004; Cheng et al., 2012; Culver et al., 2003; Dragojević et al., 2017; Shang et al., 2011; Zhou et al., 2006). Near-infrared (NIR) based optical imaging techniques, such as traditional diffuse optical tomography (DOT) and more recently developed diffuse correlation tomography (DCT), have been used as noninvasive bedside means for continuous

* Corresponding author.
** Corresponding author.
E-mail addresses: lei.chen@uky.edu (L. Chen), guoqiang.yu@uky.edu (G. Yu).

https://doi.org/10.1016/j.neuroimage.2019.05.047
Received 23 January 2019; Received in revised form 16 May 2019; Accepted 17 May 2019
Available online 18 May 2019

monitoring of cerebral blood oxygen saturation (StO_2) and CBF, respectively (Agochukwu et al., 2017; Buckley et al., 2014; Cheng et al., 2012; Durduran and Yodh, 2014; Huang et al., 2015c; Taber et al., 2010; Yu et al., 2003; Zhou et al., 2006). However, most DOT/DCT systems lack the combination of spatial resolution and wide field-of-view (FOV) to image spatially distributed brain functions. A few high-density DOT systems use numerous discrete sources and detectors coupled with fiber bundles to a head cap/helmet, facilitating improved spatial resolution over a large FOV and better separation of cerebral signals from overlaying scalp and skull (Eggebrecht et al., 2014; Ferradal et al., 2016; Hebden et al., 2002). However, expanding the FOV to cover a significant portion of the head introduces great challenges in high-channel-count instrumentation, fiber-optic-scalp coupling, and data quality management (Eggebrecht et al., 2014; Ferradal et al., 2016; Hebden et al., 2002; Huang et al., 2015b; Lin et al., 2014). Also, DCT devices employ a limited number of very expensive single-photon-counting avalanche photodiodes (APDs) for blood flow detection, leading to a high instrument cost and poor temporal-spatial resolution (Huang et al., 2015b; Lin et al., 2014).

Using charge-coupled devices (CCDs) with thousands of 2D array pixels, high-density sampling can be achieved quickly (Zhang, 2014). With unfocused wide-field illumination, CCDs have been used in microscopy to map 2D distributions of cerebral oxygenation (via optical intrinsic signal imaging: OIS technique) (Teichert and Bolz, 2017; Zhou et al., 2017) or CBF (via laser speckle contrast imaging: LSCI technique) (Durduran et al., 2004; Zhou et al., 2008) in cerebral cortices of rodents (mice or rats), where the scalp must be retracted to expose the skull and thicker skulls (rats) have to be thinned. In related mesoscopic imaging work, spatial frequency domain imaging (SFDI) and structured illumination DOT utilize structured wide-field illumination patterns and CCD detections to probe different depths of tissues up to a few millimeters (Cuccia et al., 2009; Gustafsson, 2005; Reisman et al., 2017). However, thus far, approaches with wide-field illumination and CCD detection have limited imaging penetration depths and thus are inadequate for noninvasive imaging of human brains including through the intact scalp and skull of neonates.

There have been recent advancements towards using focused point illumination and CCD detection of spatial diffuse speckle contrasts to facilitate rapid measurements of blood flow variations in relatively large and deep tissue volumes. These advanced techniques include diffuse speckle contrast analysis (DSCA), speckle contrast optical tomography (SCOT), and speckle contrast diffuse correlation tomography (scDCT). These technologies are inherently based on the same concept despite differences in nomenclature and technological evolution. DSCA uses optical fibers to deliver laser light and guide the detection by a camera sensor, thus enabling contact and spectroscopic (not tomographic) measurements of tissue blood flow with fiber-optic probes (Bi et al., 2013a, b; Bi et al., 2015; Seong et al., 2016). SCOT extends the concept with an analytical semi-infinite approximation for 3D image reconstruction of flow distributions in tissue-simulating phantoms and small mouse heads with retracted scalp (Dragojević et al., 2017; Varma et al., 2014). Our group has developed a noncontact reflectance-based scDCT technique (*US Patent #9861319, 2016–2036)* for 3D imaging of blood flow distributions in relatively large/deep tissue volumes with arbitrary boundaries (Huang et al., 2015a, 2017; Mazdeyasna et al., 2018). A finite-element-method (FEM)-based reconstruction has been developed to generate 3D flow images (Huang et al., 2015a, 2017; Lin et al., 2014). We have tested the scDCT system for 3D imaging of flow distributions in tissue-simulating phantoms, human forearms, human burned/wound tissues, and human mastectomy skin flaps (Huang et al., 2015a, 2017; Mazdeyasna et al., 2018). Results from these measurements indicate that the scDCT enables a fast and high-density 3D imaging of blood flow distributions with an adjustable depth ranging from 0 to 10 mm over an adjustable region of interest (ROI).

The goal of the present study was to adapt this innovative scDCT system for noninvasive, continuous, and longitudinal imaging of CBF variations in rat brain through the intact scalp and skull. In contrast to large ROIs (up to $100 \times 100\ mm^2$) used in our previous studies for imaging large and deep human tissue volumes, a smaller ROI is required for imaging relatively smaller rat heads ($\sim 20 \times 20\ mm^2$). Thus, we modified the scDCT system and optimized the data processing algorithms for imaging CBF in rats. The performance of this optimized scDCT system was tested for continuous 3D imaging of CBF variations in rats during CO_2 inhalations (increasing CBF) and during unilateral and bilateral transient ligations of carotid arteries (reducing CBF). Furthermore, 2D maps of CBF generated from the same datasets were compared to 3D images to evaluate the impact of partial volume effects from the top layer of scalp and skull on deep brain signals. In addition, the longitudinal imaging capability was examined by intermittent monitoring of CBF variations in a rat over a 14-day recovery period after 1-h ischemia-reperfusion stroke. To the best of our knowledge, this paper reports the *first* noncontact 3D tomographic system that enables continuous and longitudinal 3D imaging of regional CBF distributions and variations in rat brain through intact scalp and skull.

2. Methods

2.1. Modified scDCT system

2.1.1. scDCT prototype and modification

Details for the scDCT prototype can be found in our previous publications (Huang et al., 2015a, 2017; Mazdeyasna et al., 2018; Yu et al., 2018). Fig. 1 shows the scDCT system for noncontact imaging of CBF in rats. Briefly, a galvo mirror (GVS002, Thorlabs) was used to deliver point NIR light generated from a long coherence laser (785 nm, CrystaLaser) to multiple positions (Fig. 1a and b). An Electron Multiplying CCD (EMCCD) (Pixels: 1002×1004; Cascade 1K, Photometrics) was used to detect spatial speckle contrasts in a selected ROI (Fig. 1c). A long-pass filter (>750 nm, EdmundOptics) was installed in front of the EMCCD to minimize the influence of ambient light. A pair of polarizers (LPNIRE050-B and LPNIRE200-B, Thorlabs) was added crossing the source and detection paths to reduce the source reflection directly from the tissue surface. A zoom lens (Zoom 7000, Navitar) was connected to the EMCCD camera for adjusting the size of the ROI. The fully noncontact probe was fixed on a 360° rotating holder for easy adjustment and alignment. All measurements in this study utilized an exposure time of 5 ms, and the F-number of the detection zoom lens was set as 11 to meet the Nyquist sampling rule (Boas and Dunn, 2010).

In this study, the scDCT prototype was downscaled for imaging the small rat head with a limited area of $\sim 20 \times 20\ mm^2$ (Fig. 1c). A major challenge in this downscaling was to achieve a sufficient spatial sampling density (i.e., with enough source-detector pairs) over a small ROI while maintaining good signal-to-noise ratios (SNRs). For this purpose, a lever-actuated iris (SM05D5, Thorlabs) was installed in the source path (Fig. 1b) and the iris was opened approximately one half of its full aperture (diameter = 3.5 mm) to confine the light spot diameter to be less than 0.5 mm. This modification allowed the scDCT to have a sufficient number of source positions (without any overlaps across sources) distributed over a small ROI. Furthermore, the exposure time of EMCCD camera (5 ms) was optimized based on our phantom test results (Supplementary Fig. 1) to obtain effective source-detector (S-D) separations ranging from 2 to 8 mm over the small ROI (Fig. 3 and Supplementary Fig. 2).

2.1.2. Data acquisition and processing

Fig. 2 shows the flowchart for data acquisition and processing to obtain relative CBF (rCBF). To trade off temporal and spatial resolution, 25 source positions (5×5) were selected to cover a ROI of $\sim 20 \times 20\ mm^2$ on the rat head. The total sampling time for scanning over the 25 source positions was 20 s. The scDCT data were continuously collected via sequencing the source positions (adjusting the galvo mirror electronically), and two frames were taken at each source location for

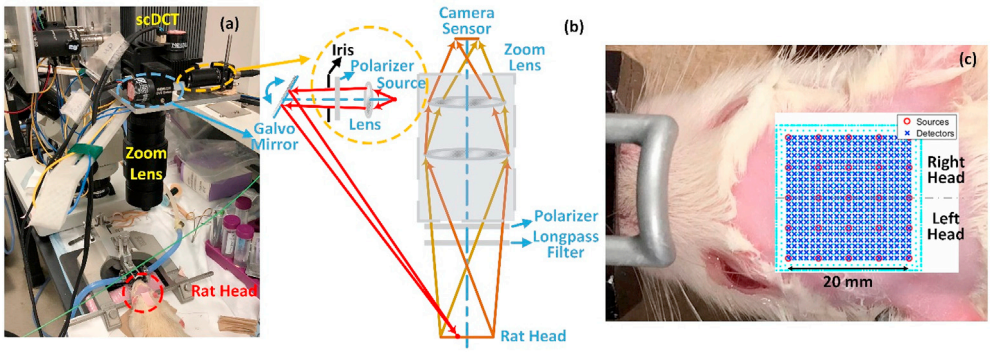

Fig. 1. A modified scDCT system for imaging of CBF in rats. (a) Experimental setup for noncontact cerebral imaging of a rat. (b) Optical design of the modified scDCT. An iris was used to limit the size of light spot. (c) Rat head hair was shaved and removed with hair cream to expose a ROI of 20 × 20 mm^2 on the rat head. 5 × 5 sources (circles) and 21 × 21 detectors (crosses) were evenly distributed within the ROI to acquire boundary flow data for 3D image reconstruction.

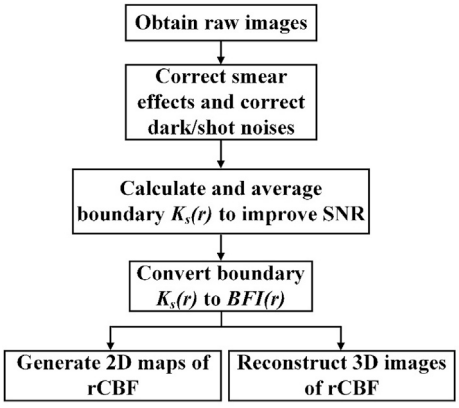

Fig. 2. Data processing flowchart for generating 2D and 3D images of rCBF.

averaging to improve SNRs.

Raw images were first preprocessed to correct sources of EMCCD camera noise including the dark noise, shot noise, and smear effect (Huang et al., 2015a, 2017). The speckle contrast $K_s(\boldsymbol{r})$ was quantified by calculating the ratio of spatial standard deviation (σ_s) and mean intensity I: $K_s(\boldsymbol{r}) = \sigma_s/I$, in a pixel window of 7 × 7 pixels on the EMCCD camera. $K_s(\boldsymbol{r})$ values were then averaged over 3 × 3 adjacent pixel windows in an area of 0.04 × 0.04 mm^2 (as a single detector) to improve detection SNRs. The scDCT collected speckle contrast data ($K_s(\boldsymbol{r})$) at all S-D pairs on the tissue surface (i.e., tissue boundary). The spatial resolution depends on the sampling density on tissue boundary, i.e., the number of S-D pairs per unit area. Averaging more pixel windows would result in one detector with a larger detection area (associated with a higher SNR) but a lower detection density (associated with a lower spatial resolution). A blood flow index ($BFI(\boldsymbol{r})$) on the tissue boundary was then extracted through the nonlinear relation between the boundary $BFI(\boldsymbol{r})$ and $K_s(\boldsymbol{r})$, measured by a defined detector. Derivation of this nonlinear relation can be found in our recent publication (Huang et al., 2017).

2.1.3. 2D mapping of CBF

The boundary BFIs were normalized to their baseline values to obtain rCBF. 2D images were generated by simply averaging boundary rCBF data obtained from the effective S-D separations of 2–8 mm, which were determined experimentally on standard homogenous tissue-simulating phantoms (see Section 2.2.1). To balance the spatial resolution and computation time for 2D mapping, 81 × 81 detectors (not shown in Fig. 1c) were selected over the ROI with the effective S-D separations ranging from 2 to 8 mm. The time to compute a 2D image was less than 10 s.

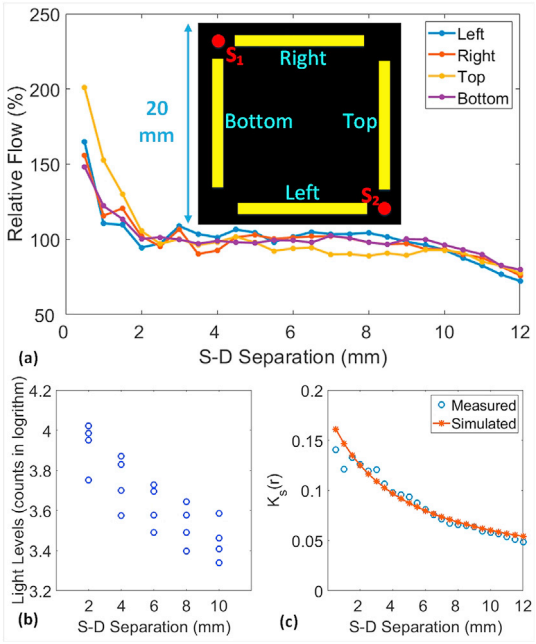

Fig. 3. (a) Boundary flow distributions over the selected sources (S_1 and S_2) and detector arrays. Each detector array consisted of 24 detectors and S-D separations ranged from 0.5 to 12 mm with an interval distance of 0.5 mm. Flow indices were normalized to their mean value to generate relative flow values for presentation. (b) Light intensities over the two sources (S_1 and S_2) and four detector arrays were logarithmically related to S-D separations. (c) Theoretical and measured $K_s(\boldsymbol{r})$ distributions at different S-D separations across the source S_2 and *left* detector array.

2.1.4. 3D image reconstruction of CBF

To balance the spatial resolution and computation time, 21 × 21 detectors (Fig. 1c) were defined in the selected ROI for 3D reconstruction. With this optimal configuration, the distance between two adjacent detectors was 1 mm. This allowed arrangement of 441 detectors without overlaps in the ROI on the rat head (see Fig. 1b). The boundary BFIs obtained from the effective S-D pairs (2–8 mm) were inserted into a modified NIRFAST program that was developed previously in our laboratory for expedient finite-element-method (FEM)-based scDCT tomographic reconstructions (Huang et al., 2015a, 2017; Lin et al., 2014).

The FEM based approach in NIRFAST recast the reconstruction into a nonlinear optimization problem (Dehghani et al., 2008). A median filter of level 2 was used to stabilize inherent experimental noise. The modified-Tikhonov regularization and biconjugate gradient stabilized iterative inversion scheme were implemented in NIRFAST for Jacobian

construction. A regularization value λ of 10 was selected empirically. A projection error change of <2% was set as a stopping criterion for iterations; each image was reconstructed with 6–8 iterations of the Jacobian function.

The image reconstruction was processed in a $24 \times 24 \times 15\,mm^3$ slab mesh with 1 mm distance nodes (~8K nodes in total). The computation time for a single image reconstruction was ~15 min. The rCBF distribution was calculated by normalizing the reconstructed BFIs at the mesh nodes to their baseline values before the physiological manipulation.

2.2. Experimental protocols

2.2.1. Phantom experiments to determine the effective S-D pairs for CBF imaging

The use of tissue-simulating phantoms with known optical properties is a commonly accepted strategy for optical instrument calibration and validation (Huang et al., 2015a; Irwin et al., 2011). We have previously conducted experiments in heterogeneous tissue phantoms with the scDCT system to demonstrate 3D reconstruction capabilities/sensitivities of the technique for imaging targets with flow contrasts at a maximal depth of ~10 mm (Huang et al., 2015a, 2017). In this study, homogenous Intralipid (Fresenius Kabi, Sweden) phantoms were used to calibrate effective S-D separations with the expectation that Intralipid particle flow was uniform everywhere inside the liquid solution. Brownian motion of the lipid emulsion (i.e., Intralipid particle flow) inside the liquid phantom mimics diffusive movements of red blood cells (i.e., blood flow) in a bulk tissue volume (Boas et al., 2016). In the phantom, the lipid concentration controls light scattering ($\mu_s^{'}$) while the concentration of India ink (Black India, MA) controls light absorption (μ_a). Optical properties of the homogeneous phantom were initially set as $\mu_a = 0.025\,cm^{-1}$ and $\mu_s^{'} = 8\,cm^{-1}$ to match realistic tissues (Huang et al., 2015a, 2017). The homogeneous liquid phantom with a constant Intralipid particle flow was measured by the scDCT and boundary flow indices measured at different S-D pairs were evaluated to determine valid S-D separations for generating a stable/constant flow index.

2.2.2. Continuous imaging of rCBF variations in rats during CO_2 inhalations

All experimental procedures involving animals were approved by University of Kentucky Institutional Animal Care and Use Committee (IACUC). Nine adult male Sprague-Dawley rats (2–3 months) were imaged (Rat #1 to #9). The noncontact scDCT probe was set above the rat head for continuous imaging of rCBF distributions before, during, and after a 10% CO_2/90% O_2 stimulation for ~10 min (Kagstrom et al., 1983; Maggio et al., 2014; Ursino and Lodi, 1998; Wagerle and Mishra, 1988). CO_2 is a well-known vascular dilator, leading to CBF increase. Each rat was anesthetized with 1–2% isoflurane and placed on a heating blanket, and its head was fixed in a stereotaxic frame. Rat head hair was shaved with a clipper and cleaned with hair cream (Fig. 1c). After ~4-min baseline recording of scDCT data, the mixed gas of 10% CO_2 and 90% O_2 was administered through a rat nose cone using Matheson Mixer Rotameter for ~10 min. CO_2 was then stopped, and scDCT measurements lasted for another ~10 min to record CBF recovery. The rat was then returned to the cage for full recovery.

2.2.3. Continuous imaging of rCBF variations in rats during transient artery ligations

The nine rats used in the CO_2-inhalation experiment underwent transient bilateral ligations of common carotid artery (CCA) to create sequential decreases in CBF within the left and right cerebral hemispheres. One rat (Rat #9) was excluded from this protocol because of a surgical complication. The hair at cervical surgical site was shaved and removed with hair cream, and all other preparations were the same as described above. For CCA ligations, the cervical skin was disinfected with Betadine followed by 70% Ethanol. A midline incision was performed to expose and isolate both the left and right CCAs. A 6-0 braided nylon suture was placed around each CCA with a loose knot. After a baseline scDCT measurement for ~2 min, the left suture was tightened to ligate the left CCA for ~10 min. The right CCA was then also ligated to induce bilateral occlusion of the CCAs for another ~2 min. Finally, the ligation of right CCA was released and scDCT measurements continued for another ~2 min to record CBF recovery. During the scDCT measurement, surgical light was removed from the detection field to reduce light interference.

2.2.4. Longitudinal imaging of rCBF variations in a rat with stroke

To test the capability of scDCT for longitudinal monitoring of rCBF variations, one additional rat (Rat #10) undergoing a transient middle cerebral artery occlusion (MCAO) of the left hemisphere was imaged intermittently before, during and after stroke over a period of 14 days. The animal preparation for each scDCT measurement was the same as described above. For MCAO, the left CCA was exposed and isolated. A silicon-rubber coated 5-0 nylon filament was inserted through internal carotid artery (ICA) and advanced 15 mm beyond the bifurcation of external carotid artery and ICA, to occlude the middle cerebral artery branching domain in the Circle of Willis or until a firm resistance was felt. Sixty minutes after left MCAO occlusion, the filament was withdrawn allowing for cerebrocortical reperfusion. The scDCT data was recorded immediately before and after inserting and withdrawing the filament at Day 0. For longitudinal monitoring, repeated scDCT measurements were performed at post-surgery days of 1, 3, 5, 9, and 14. Each measurement lasted for ~2 min and acquired CBF images were averaged for data analysis and reporting.

2.3. Statistical tests

Paired t-tests were used to evaluate differences in rCBF variations between different phases of stimuli (CO_2 inhalations and artery ligations) and spatial differences in rCBF variations between different layers of head tissues (i.e., scalp/skull versus cerebral cortex) or different hemispheres. $p < 0.05$ was considered statistically significant. In addition, the Hedges' g for paired data was calculated as a measure of effect size (ES) to quantify the magnitude of difference between groups (Gibbons et al., 1993). The corresponding 95% confidence interval (CI) was also calculated. An $ES > 0.8$ was considered as a large magnitude of difference (Cohen, 1988).

3. Results

3.1. Effective S-D pairs determined by tissue-simulating phantom experiments

A homogenous phantom with constant Intralipid particle flow was used to evaluate and calibrate the modified scDCT instrument. Fig. 3a illustrates S-D arrangements including four detector arrays (yellow bars) near the selected two sources (S_1 and S_2) over a ROI of 20 mm × 20 mm. The *right* and *bottom* detector arrays were linked to S_1 and the *left* and *top* detector arrays were linked to S_2. Each detector array consisted of 24 detectors, which were 0.5–12 mm away from the source center with an interval of 0.5 mm. The relative flow values of Intralipid particles inside the liquid solution (Fig. 3a) were generated by normalizing flow indices at different S-D separations to their mean value as the reference. Thus, the observed stable/constant flow values at the effective S-D separations of 2–8 mm were with respect to other S-D separations. Means ± standard deviations of relative flow values were 104 ± 10%, 103 ± 15%, 95 ± 8%, and 99 ± 5% for left, right, top, and bottom detector arrays, respectively. Similar results were observed from other S-D links with the same range of S-D separations (i.e., from 2 to 8 mm) at different locations (data not shown). Fig. 3b illustrates the linear relation between the logarithmic scale of light intensities (counts) and S-D separations over the two sources (S_1 and S_2) and four detector arrays. Fig. 3c shows theoretical and measured $K_s(\boldsymbol{r})$distributions at different S-D separations across the source

S_2 and *left* detector array. These results suggest that data obtained from the effective S-D separations of 2–8 mm matched expectations.

3.2. CBF responses in rats during CO_2 inhalations

Fig. 4a shows a white light image of the rat head (hair was removed) with a dotted line representing the middle line of rat head. Fig. 4b and c show typical 2D blood flow maps and corresponding time-course changes in rCBF before, during, and after CO_2 inhalation in one rat (Rat #5). Fig. 4d displays average time-course changes in rCBF over 9 rats. Table 1 summarizes rCBF changes and corresponding p and ES (with 95% CI) values at different phases of CO_2 stimulation, relative to their baseline values before CO_2 inhalation (assigned as '100%'). As expected, a significant increase in rCBF (mean ± standard error: 115 ± 7%, $p < 10^{-3}$; ES = 2.19, 95% CI = 0.93 to 3.46) over all subjects was observed during CO_2 inhalation compared to its baseline value.

Fig. 5a shows the cross-sectional views of 3D images at the depths of 0.5 mm and 3.0 mm, respectively, reconstructed from the same rat (Rat #5). Based on the photon diffusion theory, penetration depth of NIR light into biological tissues is approximately one half of the S-D separation distance (Irwin et al., 2011). Due to the limited size of the ROI on a small rat head, the effective S-D separations of the modified scDCT ranged from 2 to 8 mm. According to the anatomy of the rat head (0.5 mm scalp thickness and 1 mm skull thickness) (Nowak et al., 2011), a penetration depth of 3 mm should reach the surface of rat brain cortex while a depth of 0.5 mm should reach the rat scalp/skull. Fig. 5b and c show the time-course of rCBF during CO_2 inhalation in both layers of Rat #5 and over all 9 rats, respectively. The summary of rCBF changes in different layers is also included in Table 1. Significant increases in blood flow were observed at both depths of 0.5 mm (118 ± 8%; $p < 10^{-3}$; ES = 2.16, 95% CI = 1.73 to 4.68) and 3.0 mm (119 ± 8%; $p \leq 10^{-3}$; ES = 2.30, 95% CI = 1.01 to 3.60), while no significant differences were observed between the two layers (p = 0.60). There tended to be a difference between layers during the recovery stage (p = 0.02; ES = 0.93, 95% CI = −0.11 to 1.99). These results verified that CO_2 worked as a vascular dilator to induce a global increase of blood flow in both scalp/skull and brain tissues.

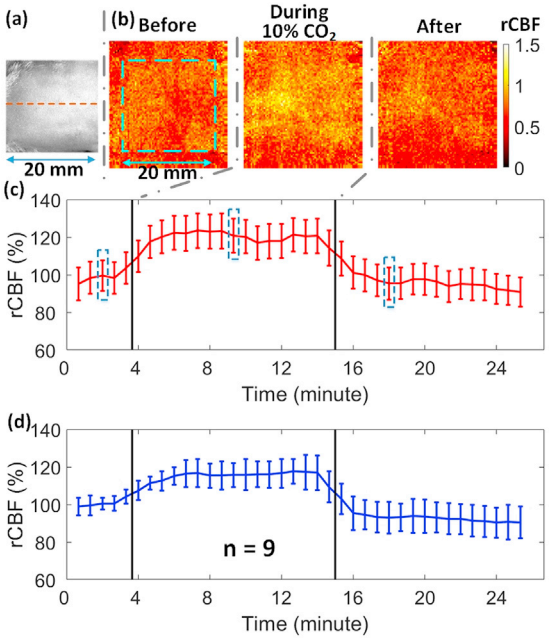

Fig. 4. 2D mapping of rCBF responses to CO_2 inhalation. (a) A white light photo of the rat head (hair was removed) with a dotted line representing the midline. (b) 2D rCBF maps before, during and after CO_2 inhalation in an illustrative rat (Rat #5). The dimension of the dashed box (20 mm × 20 mm) is the same as (a). (c) Time-course rCBF variations in two hemispheres from Rat #5. Error bars represent standard deviations of regional rCBF. The blue dashed boxes represent the time of the images in Fig. 4b. Same in following figures. (d) Average time-course of rCBF variations over 9 rats. Error bars represent standard errors of regional rCBF over 9 rats.

Table 1
rCBF changes induced by CO_2 inhalations compared to their baselines (100%) over 9 rats. Bolded differences are insignificant.

9 Rats		CO_2 Inhalation	Recovery
3D Images	2D Maps	115 ± 7% $p < 10^{-3}$; ES = 2.19 (0.93, 3.46)	93 ± 8% p = 0.06; ES = 0.70 (−0.32, 1.73)
	0.5 mm Layer	118 ± 8% $p < 10^{-3}$; ES = 2.16 (1.73, 4.68)	98 ± 8% p = 0.40; ES = 0.18 (−0.81, 1.18)
	3.0 mm Layer	119 ± 8% $p < 10^{-3}$; ES = 2.30 (1.01, 3.60)	102 ± 5% p = 0.25; ES = 0.39 (−0.61, 1.40)
	Between Layers	p = 0.60; ES = 0.17 (−0.82, 1.17)	p = 0.02; ES = 0.93 (−0.11, 1.99)

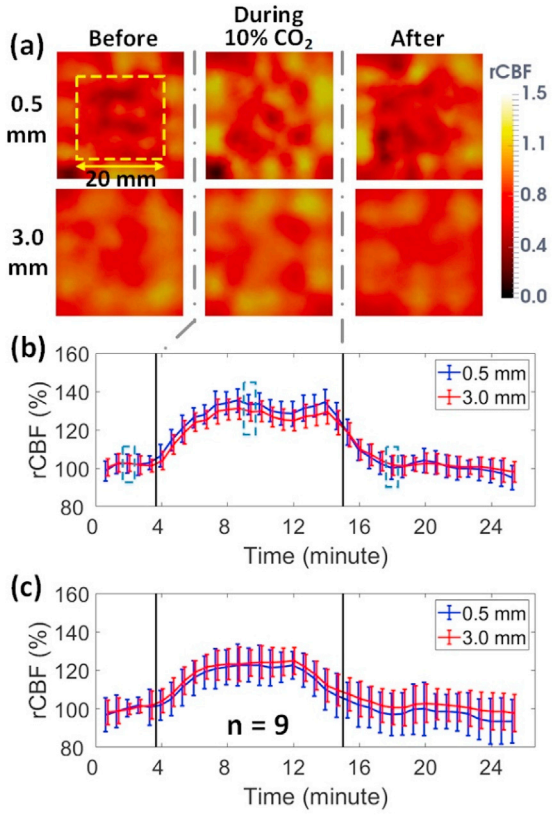

Fig. 5. 3D imaging of rCBF responses to CO_2 inhalation. (a) Cross-sectional views of 3D flow images at the depths of 0.5 mm (scalp/skull) and 3.0 mm (cerebral cortex) before, during, and after CO_2 inhalation in an illustrative rat (Rat #5). (b) Time-course of rCBF changes at two depths from Rat #5. Error bars represent standard deviations of regional rCBF. (c) Average time-course rCBF variations over 9 rats. Error bars represent standard errors of regional rCBF over 9 rats.

3.3. CBF responses in rats during unilateral and bilateral CCA ligations

Fig. 6a and Fig. 6b show typical 2D blood flow maps in a rat (Rat #3) and the corresponding time-course for rCBF across different phases of CCA ligations, including baseline, left-ligation, bilateral-ligation, and the release of right-ligation. Fig. 6c displays average time-course changes in

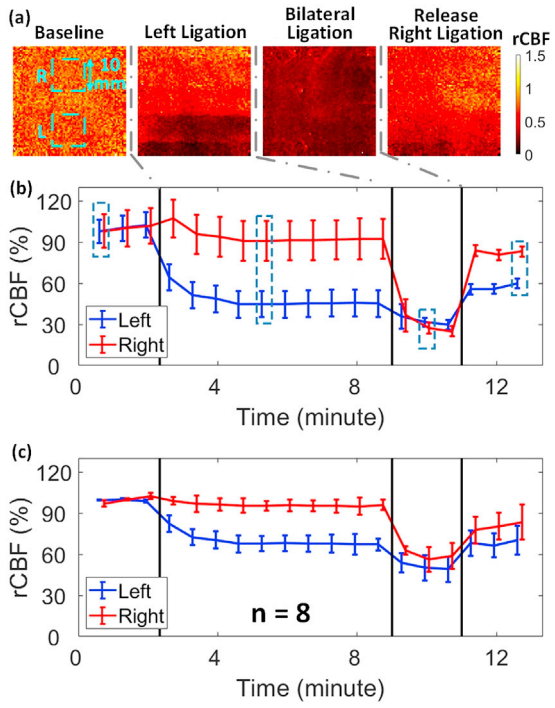

Fig. 6. 2D mapping of rCBF responses to sequential unilateral and bilateral CCA ligations. (a) 2D rCBF maps before, during, and after unilateral and bilateral ligations in an illustrative rat (Rat #3). The $10 \times 10\,mm^2$ regions used to average CBF values corresponding to each hemisphere are marked with dashed squares. (b) Time-course of rCBF variations in two hemispheres from Rat #3. Error bars represent standard deviations of regional rCBF. (c) Average time-course of rCBF variations in each hemisphere for 8 rats. Error bars represent standard errors of regional rCBF over 8 rats.

rCBF over 8 rats. Table 2 summarizes rCBF changes and corresponding p and ES (with 95% CI) values at different phases of ligations. Significant differences in rCBF from baseline were observed in both the left and right hemispheres at all stages of ligations ($p \leq 0.01$). The unilateral (left) ligation and the recovery stage (release of right ligation) resulted in significantly different rCBF responses between the two hemispheres ($p \leq 0.002$). All of these significant differences had large ES (Table 2). rCBF was not significantly different between the two hemispheres during the bilateral ligation ($p = 0.051$).

Fig. 7a shows the cross-sectional views of 3D images at the depths of 0.5 mm and 3.0 mm, reconstructed from the same rat (Rat #3). As stated, these two depths (0.5 mm and 3.0 mm) beneath the head skin represent the tissues in the scalp/skull and cerebral cortex, respectively. The time-course of changes in rCBF over different phases of ligations in both layers of each hemisphere is illustrated for Rat #3 (Fig. 7b) and for all 8 rats (Fig. 7c). The summary of rCBF changes in different layers of each hemisphere is also included in Table 2. As expected, sequential CCA ligations (i.e., left ligation followed by bilateral ligation) resulted in stepwise rCBF decreases in the corresponding ligated hemisphere(s). Significant changes in rCBF were found at all stages of ligations in both layers of the ligated hemisphere(s) ($p < 10^{-3}$). In contrast, there were no significant changes in the surface layer of the contralateral (right) hemisphere during stages of unilateral (left) ligation ($p = 0.06$ and $p = 0.054$), likely due to the collateral circulation through the Circle of Willis. However, significant rCBF decreases were observed in the deep layers of the right hemisphere ($p < 10^{-3}$) during bilateral ligations, indicating global ischemia. Moreover, significant rCBF differences were observed between the two hemispheres during the unilateral ligation and recovery stages ($p < 10^{-3}$) and between the two layers ($p \leq 0.03$). All the observed significant differences had large ES (Table 2). As with the 2D image analysis, rCBF was not significantly different between the two hemispheres during bilateral ligation when analyzed from 3D images at either depth ($p = 0.45$ and $p = 0.56$).

3.4. Longitudinal CBF responses to unilateral MCAO in a rat

3D images of CBF variations in a rat (Rat #10) before, during, and 14 days after 60-min unilateral MCAO were reconstructed using the same method described above (data not shown). Fig. 8 shows the time-course of rCBF changes before, during, and after MCAO-induced stroke in two

Table 2
rCBF changes during unilateral and bilateral CCA ligations compared to their baselines (100%) over 8 rats. Bolded differences are insignificant.

8 Rats			Left Ligation	Bilateral Ligation	Release Right Ligation
2D Maps		Left	69 ± 4% $p < 10^{-3}$; ES = 7.01 (4.15, 9.88)	50 ± 5% $p < 10^{-3}$; ES = 9.82 (5.94, 13.70)	66 ± 5% $p < 10^{-3}$; ES = 6.21 (3.62, 8.79)
		Right	95 ± 3% p = 0.01; ES = 1.15 (0.01, 2.31)	56 ± 5% $p < 10^{-3}$; ES = 7.71 (4.59, 10.82)	80 ± 6% $p < 10^{-3}$; ES = 3.31 (1.66, 4.96)
		Between Hemispheres	$p < 10^{-3}$; ES = 4.21 (2.28, 6.13)	p = 0.051; ES = 0.78 (−0.32, 1.90)	p = 0.002 ES = 1.52 (0.30, 2.74)
3D Images	0.5 mm Layer	Left	85 ± 3% $p < 10^{-3}$; ES = 5.14 (2.91, 7.37)	61 ± 7% $p < 10^{-3}$; ES = 5.39 (3.08, 7.70)	62 ± 9% $p < 10^{-3}$; ES = 4.09 (2.20, 5.98)
		Right	95 ± 4% p = 0.06; ES = 1.01 (−0.12, 2.15)	58 ± 7% $p < 10^{-3}$; ES = 5.89 (3.41, 8.37)	93 ± 8% p = 0.054; ES = 0.81 (−0.29, 1.93)
		Between Hemispheres	$p < 10^{-3}$; ES = 3.09 (1.50, 4.68)	p = 0.45; ES = 0.26 (−0.81, 1.34)	$p < 10^{-3}$; ES = 4.16 (2.25, 6.07)
	3.0 mm Layer	Left	35 ± 9% $p < 10^{-3}$; ES = 7.09 (4.19, 9.98)	32 ± 11% $p < 10^{-3}$; ES = 6.04 (3.51, 8.57)	41 ± 12% $p < 10^{-3}$; ES = 4.56 (2.52, 8.59)
		Right	84 ± 6% $p < 10^{-3}$; ES = 2.61 (1.15, 4.07)	34 ± 10% $p < 10^{-3}$; ES = 6.05 (3.52, 8.59)	84 ± 11% p = 0.003; ES = 1.42 (0.22, 2.62)
		Between Hemispheres	$p < 10^{-3}$; ES = 4.50 (2.48, 6.52)	p = 0.56; ES = 0.20 (−0.87, 1.27)	$p < 10^{-3}$; ES = 2.22 (0.85, 3.58)
	Between Layers	Left	$p < 10^{-3}$; ES = 5.49 (3.15, 7.84)	$p < 10^{-3}$; ES = 2.22 (0.86, 3.59)	p = 0.007; ES = 1.25 (0.08, 2.43)
		Right	$p < 10^{-3}$; ES = 2.27 (0.89, 3.64)	$p < 10^{-3}$; ES = 2.00 (0.68, 3.31)	p = 0.03; ES = 2.22 (0.85, 3.58)

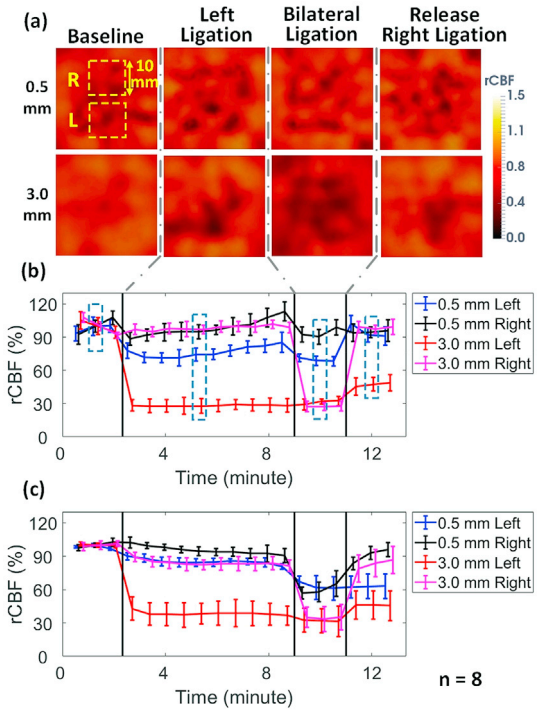

Fig. 7. 3D imaging of rCBF responses to sequential unilateral and bilateral CCA ligations. (a) Cross-sectional views of 3D flow images at the depths of 0.5 mm (scalp/skull) and 3.0 mm (cerebral cortex) before, during, and after unilateral and bilateral ligations in an illustrative rat (Rat #3). The $10 \times 10\ mm^2$ regions used to average CBF values corresponding to each hemisphere are marked with dashed squares. (b) Time-course of rCBF variations in two hemispheres from Rat #3. Error bars represent standard deviations of regional rCBF. The dashed boxes represent the time of the images in Fig. 7a. (c) Average time-course of rCBF variations in two hemispheres over 8 rats. Error bars represent standard errors of regional rCBF over 8 rats.

layers (0.5 mm and 3.0 mm) for each hemisphere. Substantial rCBF decreases were observed in the two layers of ipsilateral side after inserting the filament into left internal carotid artery, especially in the brain layer (−70%). After withdrawing the filament, rCBF recovered gradually toward its baseline. From 9 to 14 days after stroke, rCBF values in different layers of two hemispheres tended to be similar, although they were still lower than the pre-stroke values.

4. Discussion and conclusions

We have modified, optimized, and tested a fully noncontact scDCT system that allows for noninvasive, continuous, and longitudinal imaging of CBF variations in rat brain through intact scalp and skull (Fig. 1). In scDCT, a galvo mirror is used to remotely and rapidly project point NIR light to different source positions and an EMCCD camera with numerous pixels/detectors is used to detect boundary diffuse speckle contrasts resulting from motion of red blood cells (i.e., CBF). The focused NIR point source illuminations facilitate relatively deep probing into rat brain through intact scalp and skull. In addition, thousands of parallel pixels/detectors provided by the EMCCD camera significantly improve SNRs (via averaging pixels/detectors) and temporal/spatial resolution, and greatly reduce device cost and dimensions. The scDCT measurement allows a fully noncontact scheme, avoiding the difficulties of fiber-optic probe installation on a small rat head and eliminating potential disturbances in cerebral hemodynamics due to probe contact. The noninvasive, noncontact, and easy-to-operate capability of scDCT is particularly useful for continuous, frequent, and longitudinal cerebral monitoring. Moreover, scDCT works in the reflectance configuration with an adjustable ROI, rapid and robust data acquisition, and flexible S-D arrangements. The reflectance-based operation increases the applicability of scDCT to large subjects (e.g., human neonates) where transmission is not feasible, thereby promoting translatability between small animals and human subjects.

The scDCT system has been optimized for continuous cerebral imaging in rats. To image a rat head with a small detection area ($20 \times 20\ mm^2$), an adjustable iris diaphragm was added into the source path to optimize the intensity and spot size of incident light. To balance temporal and spatial resolution, reduce computation time, and achieve sufficient SNRs, the numbers of sources and detectors were optimized for 2D and 3D imaging. In 3D reconstruction, we optimized the parameters/configuration in NIRFAST, including medium filter, mesh/node size, regularization value, and stopping criteria. In 2D mapping, we averaged boundary data collected at the effective S-D separations of 2–8 mm to generate a 2D map over a depth up to ~4 mm (i.e., approximately one half of the S-D separation).

To calibrate the modified scDCT system, homogenous Intralipid phantoms were used to optimize camera exposure time and determine effective S-D separations with the expectation that Intralipid particle flow was uniform in the liquid solution (Fig. 3). The scDCT technique inherits the concept of LSCI for blood flow measurements on a tissue surface. A previous study has experimentally compared measurement sensitivities and SNRs of LSCI with exposure times ranging from 1 to 20 ms (Yuan et al., 2005), and verified the optimal exposure time of 5 ms. Similarly, we have compared our scDCT measurement results in homogenous tissue phantoms at exposure times of 1, 2, and 5 ms (see Supplementary Fig. 1). Data obtained with the exposure time of 5 ms generate the most stable/constant relative flow values at effective S-D separations of 2–8 mm. To test the dependence of effective S-D separations on phantom optical properties, we used the scDCT to measure particle flow changes due to varied temperatures (Supplementary Fig. 2a) and varied tissue absorption coefficient μ_a by adding Indian ink (Supplementary Fig. 2b). All results shown in Fig. 3 and Supplementary Figures verify that data obtained at S-D separations of 2–8 mm are constant and stable.

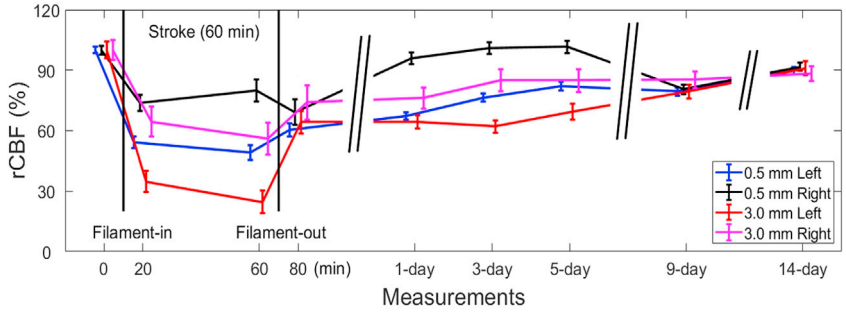

Fig. 8. Longitudinal monitoring of rCBF responses to unilateral MCAO. Time-course of rCBF changes at the depths of 0.5 mm (scalp/skull) and 3.0 mm (cerebral cortex) of both hemispheres in a rat (Rat #10) before, during, and until 14 days after MCAO-induced stroke in the left hemisphere. Error bars represent standard deviations of regional rCBF.

The larger flow variation observed at shorter S-D separations of <2 mm is likely due to the violation of photon diffusion approximation. The greater flow variation observed at larger S-D separations of >8 mm is likely due to lower level of SNRs (with lower light intensities detected). Using boundary data at short S-D separations of 2–8 mm may cause reconstruction errors due to violation of photon diffusion approximation in NIRFAST. However, our results in phantom tests (Fig. 3) and *in vivo* studies (Figs. 5 and 7) demonstrate the success of scDCT in 3D reconstruction of flow distributions. In addition, previous studies with conventional DCT or SCOT have also used short S-D separations of 2.7–10 mm (Culver et al., 2003) or 0.5–3 mm (Dragojević et al., 2017) for 3D imaging of CBF distributions in rats or mice.

After calibrating the modified scDCT system using standard tissue-simulating phantoms (Fig. 3), we tested the capability and sensitivity of scDCT for continuous and longitudinal monitoring of global/regional cerebral hyper-perfusion/hypo-perfusion and post-operation recovery in rats undergoing transient cerebral hyperemia (via CO_2 inhalation) and cerebral ischemia (via CCA ligations or MCAO). The 10% CO_2 inhalation induced significant increases in rCBF from the baseline of 100% of 15% ($115 \pm 7\%$) in 2D maps and 18% ($118 \pm 8\%$) and 19% ($119 \pm 8\%$) in the superficial (scalp/skull) and deep (brain) layers of 3D images, respectively (Figs. 4 and 5, and Table 1). These results are expected in a healthy population, as the increased CO_2 induces cerebrovascular dilation, leading to a global increase in blood flow all over the head. The small variation in rCBF increases between the results in 2D and 3D images (from +15% to +19%) was likely due to differences in methodology (i.e., 2D versus 3D).

Previously, 10% CO_2 inhalation induced a $47 \pm 11\%$ CBF increase in 7 rats measured by arterial-spin-labeling (ASL)-MRI (Sicard et al., 2003) and a $35.1 \pm 6.3\%$ CBF increase in 11 rats measured by laser Doppler flowmetry (LDF) (Wolk et al., 1995). Another study using diffuse correlation spectroscopy (DCS) found an ~25% CBF increase in 7 rats with a continuous inhalation of 5%–7.5% CO_2 for ~10 min (Carp et al., 2010). We found in the present study that 10% CO_2 inhalation for 10 min induced a $19 \pm 8\%$ CBF increase in 9 rats (Table 1). The CBF responses to CO_2 inhalation measured by the DCS (~+25%) and scDCT (~+19%) are similar. Comparing to measurements by ASL-MRI (~+47%) and LDF (~+35%), an underestimation of CBF increases by DCS and scDCT (<~25%) was likely due to partial volume effects from the overlaying skull (lack of blood flow) on CBF measurements. In the future, we will explore optimizing 3D reconstruction algorithms (e.g., adding sensitivity correction factors along depths) to further reduce this effect/artifact (Tian and Liu, 2014). Moreover, we will implement blood gas tests in our future studies to further verify CBF measurement results. However, our noninvasive and portable scDCT has obvious advantages over ASL-MRI (large and expensive instruments) as well as LDF and DCS (spectroscopic measurements with invasive retraction of scalp/skull).

The capability of scDCT for continuous imaging of regional rCBF variations was then examined in rats undergoing sequential unilateral and bilateral CCA ligations. The unilateral left-CCA ligation created significant decreases in ipsilateral (left) rCBF from the baseline of 100% of 31% (to $69 \pm 4\%$) in 2D maps and 15% (to $85 \pm 3\%$) in the superficial layer (scalp/skull) and 65% (to $35 \pm 9\%$) in the deep (brain) layer of 3D images (Figs. 6 and 7, and Table 2). The sequential bilateral CCA ligation induced greater decreases in rCBF: 50% (to $50 \pm 5\%$) and 44% (to $56 \pm 4\%$) within the left and right hemispheres, respectively, in 2D maps. Similar left and right hemispheric rCBF decreases were measured from 3D images: 39% (to $61 \pm 7\%$) and 35% (to $65 \pm 10\%$) in the superficial layer (scalp/skull) and 68% (to $32 \pm 11\%$) and 66% (to $34 \pm 10\%$) in the deep (brain) layer. Our reconstructed 3D images covered depths spanning from superficial skull and scalp to deeper cerebral cortex. Since the top layers of skull and scalp were less affected by the CCA ligations due to collateral supply from the vertebral artery, smaller CBF decreases were observed in the top scalp/skull layer compared to the deeper brain layer. Compared to 3D reconstruction results, 2D mapping resulted in an underestimation of rCBF responses in deep brain tissues and an overestimation in top scalp/skull tissues (i.e., partial volume effects). This is not surprising as results from 2D mapping are overlapped mixture signals from the top scalp/skull to the deeper brain. Partial volume effects were also observed in 2D mapping of CBF responses in the control (right) hemisphere without ligation (Table 2). Nonetheless, significant rCBF differences were observed between the two hemispheres in both 2D maps and 3D images and between the two layers in 3D images, indicating the sensitivity of scDCT in detecting regional cerebral hypoperfusion and recovery.

A few studies using LDF (Alkayed et al., 1998; Takahashi et al., 1997) or conventional DCT (Culver et al., 2003) have monitored CBF reductions in rats with acute cerebral artery occlusions. Previously using LDF, Alkayed et al. and Takahashi et al. found that CBF levels were reduced during acute MCAO from 100% baseline to $18.9 \pm 1.4\%$ in 22 rats and $20.8 \pm 7.7\%$ in 5 rats, respectively (Alkayed et al., 1998; Takahashi et al., 1997). Using a convetional DCT system, Culver et al. found that CBF levels were reduced from 100% baseline to $42 \pm 4\%$ in 5 rats during acute MCAO (Culver et al., 2003). In the present study with scDCT, we observed CBF reductions of ~65% (to $35 \pm 9\%$) in 8 rats during acute unilateral CCA ligation and 70% in one rat during acute MCAO (see Figs. 6–8 and Table 2). Note that both unilateral CCA ligation and MCAO cut off the CBF in one hemisphere of brain. In summary, the observed CBF reductions due to acute arterial occlusions were ~80% (LDF), ~65–70% (scDCT), and ~60% (conventional DCT). It is not surprising that LDF detected the greatest CBF reduction (80%) as the probe was installed directly on the cerebral cortex where the most severe ischemia occurred (eliminating any partial volume effects). Comparing to conventional DCT with limited numbers of sources and detectors (Culver et al., 2003), our scDCT with higher sampling densities provided by the EMCCD camera generated results with less partial volume effects from the overlaying scalp and skull on CBF measurements. Overall, our fully noninvasive scDCT achieved a similar level of sensitivity/accuracy in detecting CBF reductions in ischemic rat brains as other conventional techniques such as LDF and DCT, which require invasive scalp retraction.

The last experiment was designed to test the capability of scDCT for longitudinally monitoring CBF variations in a rat undergoing unilateral MCAO and long-term recovery after acute stroke. A substantial decrease in rCBF (70%) was observed in the brain layer of the ipsilateral hemisphere during a unilateral 60-min MCAO (Fig. 8). After withdrawal of the filament to restore cerebral perfusion, rCBF recovered gradually towards pre-stroke baseline over a period of 14 days, although it remained somewhat lower than its pre-stroke value. Differences in rCBF responses were observed between the two hemispheres and two layers over the monitoring period, indicating the sensitivity and stability of scDCT for longitudinal detection of regional cerebral hypoperfusion and recovery. The trend of rCBF recovery after stroke agrees with that measured by ASL-MRI in rats (Seevinck et al., 2010). In addition, CBF variations over the monitoring period were also associated with neurological/behavior changes. The rat demonstrated the most severe neurological deficit symptoms one day after stroke, including stiffness of forelimb and mild coordination dysfunction. The rat recovered gradually in the first week after stroke and behaved normally at post-stroke Day 14. Noninvasive and noncontact measurements with scDCT significantly reduce interference with cerebral hemodynamics and make it easy to implement for frequent and longitudinal monitoring.

As expected, 2D mapping of CBF required less computation time (e.g., ~10 s in this study), but was subject to partial volume effects from overlaying layers of scalp and skull tissues. By contrast, 3D tomography of CBF reduces partial volume effects, but needs a longer reconstruction time (e.g., ~15 min in this study). Our data shown in Fig. 7 and Table 2 support this statement. For example, CBF reductions during bilateral CCA ligations were 66% (left) to 68% (right) in the brain layers (at the depth of 3 mm) of 3D images, which were greater than the reductions of 44% (left) to 50% (right) observed in 2D maps. Note that 2D maps of CBF were calculated in this study via averaging boundary data at multiple effective S-D separations of 2–8 mm, thus representing a mixture of signals from the superficial scalp/skull to the deep brain. Therefore, our 2D mapping

method is different from the traditional LSCI technique, which uses wide-field illumination and provides 2D maps of CBF only from superficial tissues (penetration depth < 1 mm).

We note that our innovative scDCT system can be further improved in the future and extended for other applications. For example, use of a high-quality CCD or scientific complementary metal–oxide–semiconductor (sCMOS) camera with fast sampling rate and high sensitivity would improve data acquisition, detection sensitivity, and probing depth. The algorithms for 2D mapping and 3D reconstruction may be optimized to be faster (Wu et al., 2015) and more robust (e.g., with depth compensation for denoise) (Tian and Liu, 2014; Tian et al., 2010). We may also explore absolute BFI measurements by using multiple exposure times of the camera and/or multiple S-D separations (Liu et al., 2017; Valdes et al., 2014). Adding other long-coherence laser diodes at different NIR wavelengths would allow for simultaneous imaging of blood flow and oxygenation distributions (Seong et al., 2016; Shang et al., 2009).

In conclusion, we have downscaled, optimized, and tested an innovative scDCT system for noninvasive, continuous, and longitudinal imaging of CBF distributions in rat brains through intact scalp and skull. The continuous dynamic imaging capability of the system was proven by imaging global CBF increases during CO_2 inhalations and regional CBF decreases during CCA ligations. The regional imaging capability was demonstrated by imaging CBF distributions across two hemispheres of the brain during sequential unilateral and bilateral CCA ligations. The longitudinal imaging capability was shown by imaging CBF variations over a long recovery period of 14 days after MCAO-induced stroke. Both 2D and 3D images capture temporal CBF variations precisely. Compared to the 2D mapping method, the 3D imaging method reduces partial volume effects, but needs more computation time for image reconstruction. Moreover, our results generally agree with those reported using other CBF monitoring techniques in rats with similar experimental protocols. Our innovative scDCT system provides many unique advanced features including fully noncontact hardware, rapid data acquisition, adjustable S-D patterns/density over a flexible ROI/FOV, FEM-based image reconstruction, and a simple low-cost instrument. Most importantly, scDCT allows for probing depths up to ~10 mm (Huang et al., 2015a, 2017), which is sufficient for transcranial brain measurements in small animals (e.g., mouse, rat, piglet) and human neonates, who have relatively thinner skulls (Li et al., 2015; O'Reilly et al., 2011). Ultimately with more future investigations, we expect to provide a unique, noninvasive, noncontact cerebral imager for basic neuroscience research in small animal models and translational studies in human neonates.

Acknowledgment

This work was supported by the National Institutes of Health (NIH, R21-HD091118, R21-AR062356, R21-AG046762, and COBRE #1P20GM121327), American Heart Association (AHA #16GRNT30820006 and #14SDG20480186) and National Science Foundation (NSF #1539068), Biostatistics and Bioinformatics Shared Resource of the University of Kentucky Markey Cancer Center (P30CA177558). The content is solely the responsibility of the authors and does not necessarily represent the official views of the NIH, AHA, or NSF.

Appendix A. Supplementary data

Supplementary data to this article can be found online at https://doi.org/10.1016/j.neuroimage.2019.05.047.

References

Agochukwu, N.B., Huang, C., Zhao, M., Bahrani, A.A., Chen, L., McGrath, P., Yu, G., Wong, L., 2017. A novel noncontact diffuse correlation spectroscopy device for assessing blood flow in mastectomy skin flaps: a prospective study in patients undergoing prosthesis-based reconstruction. Plast. Reconstr. Surg. 140, 26–31.

Alkayed, N.J., Harukuni, I., Kimes, A.S., London, E.D., Traystman, R.J., Hurn, P.D., 1998. Gender-linked brain injury in experimental stroke. Stroke 29, 159–165 discussion 166.

Bi, R., Dong, J., Lee, K., 2013a. Deep tissue flowmetry based on diffuse speckle contrast analysis. Optic Lett. 38, 1401–1403.

Bi, R., Dong, J., Lee, K., 2013b. Multi-channel deep tissue flowmetry based on temporal diffuse speckle contrast analysis. Optic Express 21, 22854–22861.

Bi, R., Dong, J., Poh, C.L., Lee, K., 2015. Optical methods for blood perfusion measurement - theoretical comparison among four different modalities. J. Opt. Soc. Am. A 32, 860–866.

Boas, D.A., Dale, A.M., Franceschini, M.A., 2004. Diffuse optical imaging of brain activation: approaches to optimizing image sensitivity, resolution, and accuracy. Neuroimage 23, S275–S288.

Boas, D.A., Dunn, A.K., 2010. Laser speckle contrast imaging in biomedical optics. J. Biomed. Opt. 15, 011109.

Boas, D.A., Sakadzic, S., Selb, J., Farzam, P., Franceschini, M.A., Carp, S.A., 2016. Establishing the diffuse correlation spectroscopy signal relationship with blood flow. Neurophotonics 3, 031412.

Buckley, E.M., Parthasarathy, A.B., Grant, P.E., Yodh, A.G., Franceschini, M.A., 2014. Diffuse correlation spectroscopy for measurement of cerebral blood flow: future prospects. Neurophotonics 1.

Carp, S.A., Dai, G.P., Boas, D.A., Franceschini, M.A., Kim, Y.R., 2010. Validation of diffuse correlation spectroscopy measurements of rodent cerebral blood flow with simultaneous arterial spin labeling MRI; towards MRI-optical continuous cerebral metabolic monitoring. Biomed. Opt. Express 1, 553–565.

Cheng, R., Shang, Y., Hayes, D., Saha, S.P., Yu, G., 2012. Noninvasive optical evaluation of spontaneous low frequency oscillations in cerebral hemodynamics. Neuroimage 62, 1445–1454.

Chesselet, M.F., Carmichael, S.T., 2012. Animal models of neurological disorders. Neurotherapeutics 9, 241–244.

Cohen, J., 1988. Statistical Power Analysis for the Behavioral Sciences, second ed. Lawrence Earlbaum Associates, Hillsdale, NJ.

Cuccia, D.J., Bevilacqua, F., Durkin, A.J., Ayers, F.R., Tromberg, B.J., 2009. Quantitation and mapping of tissue optical properties using modulated imaging. J. Biomed. Opt. 14, 024012.

Culver, J.P., Durduran, T., Furuya, T., Cheung, C., Greenberg, J.H., Yodh, A.G., 2003. Diffuse optical tomography of cerebral blood flow, oxygenation, and metabolism in rat during focal ischemia. J. Cereb. Blood Flow Metab. 23, 911–924.

Dehghani, H., Eames, M.E., Yalavarthy, P.K., Davis, S.C., Srinivasan, S., Carpenter, C.M., Pogue, B.W., Paulsen, K.D., 2008. Near infrared optical tomography using NIRFAST: algorithm for numerical model and image reconstruction. Commun. Numer. Methods Eng. 25, 711–732.

Dragojević, T., Varma, H.M., Hollmann, J.L., Valdes, C.P., Culver, J.P., Justicia, C., Durduran, T., 2017. High-density speckle contrast optical tomography (SCOT) for three dimensional tomographic imaging of the small animal brain. Neuroimage 153, 283–292.

Durduran, T., Burnett, M.G., Yu, G., Zhou, C., Furuya, D., Yodh, A.G., Detre, J.A., Greenberg, J.H., 2004. Spatiotemporal quantification of cerebral blood flow during functional activation in rat somatosensory cortex using laser-speckle flowmetry. J. Cereb. Blood Flow Metab. 24, 518–525.

Durduran, T., Yodh, A.G., 2014. Diffuse correlation spectroscopy for non-invasive, micro-vascular cerebral blood flow measurement. Neuroimage 85 (Pt 1), 51–63.

Durukan, A., Strbian, D., Tatlisumak, T., 2008. Rodent models of ischemic stroke: a useful tool for stroke drug development. Curr. Pharmaceut. Des. 14, 359–370.

Eggebrecht, A.T., Ferradal, S.L., Robichaux-Viehoever, A., Hassanpour, M.S., Dehghani, H., Snyder, A.Z., Hershey, T., Culver, J.P., 2014. Mapping distributed brain function and networks with diffuse optical tomography. Nat. Photon. 8, 448–454.

Ellenbroek, B., Youn, J., 2016. Rodent models in neuroscience research: is it a rat race? Dis. Model. Mech. 9, 1079–1087.

Ferradal, S.L., Liao, S.M., Eggebrecht, A.T., Shimony, J.S., Inder, T.E., Culver, J.P., Smyser, C.D., 2016. Functional imaging of the developing brain at the bedside using diffuse optical tomography. Cerebr. Cortex 26, 1558–1568.

Gibbons, R.D., Hedeker, D.R., Davis, J.M., 1993. Estimation of effect size from a series of experiments involving paired comparisons. J. Educ. Stat. 18, 271–279.

Gustafsson, M.G., 2005. Nonlinear structured-illumination microscopy: wide-field fluorescence imaging with theoretically unlimited resolution. Proc. Natl. Acad. Sci. U. S. A. 102, 13081–13086.

Hebden, J.C., Gibson, A., Yusof, R.M., Everdell, N., Hillman, E.M., Delpy, D.T., Arridge, S.R., Austin, T., Meek, J.H., Wyatt, J.S., 2002. Three-dimensional optical tomography of the premature infant brain. Phys. Med. Biol. 47, 4155–4166.

Huang, C., Irwin, D., Lin, Y., Shang, Y., He, L., Kong, W., Luo, J., Yu, G., 2015a. Speckle contrast diffuse correlation tomography of complex turbid medium flow. Med. Phys. 42, 4000–4006.

Huang, C., Irwin, D., Zhao, M., Shang, Y., Agochukwu, N., Wong, L., Yu, G., 2017. Noncontact 3-dimensional speckle contrast diffuse correlation tomography of tissue blood flow distribution. IEEE Trans. Med. Imaging 36, 2068–2076.

Huang, C., Lin, Y., He, L., Irwin, D., Szabunio, M.M., Yu, G., 2015b. Alignment of sources and detectors on breast surface for noncontact diffuse correlation tomography of breast tumors. Appl. Opt. 54, 8808–8816.

Huang, C., Radabaugh, J.P., Aouad, R.K., Lin, Y., Gal, T.J., Patel, A.B., Valentino, J., Shang, Y., Yu, G., 2015c. Noncontact diffuse optical assessment of blood flow changes in head and neck free tissue transfer flaps. J. Biomed. Opt. 20, 075008.

Irwin, D., Dong, L.X., Shang, Y., Cheng, R., Kudrimoti, M., Stevens, S.D., Yu, G., 2011. Influences of tissue absorption and scattering on diffuse correlation spectroscopy blood flow measurements. Biomed. Opt. Express 2, 1969–1985.

Kagstrom, E., Smith, M.L., Siesjo, B.K., 1983. Cerebral circulatory responses to hypercapnia and hypoxia in the recovery period following complete and incomplete cerebral ischemia in the rat. Acta Physiol. Scand. 118, 281–291.

Li, Z., Park, B.K., Liu, W., Zhang, J., Reed, M.P., Rupp, J.D., Hoff, C.N., Hu, J., 2015. A statistical skull geometry model for children 0-3 years old. PLoS One 10 e0127322.
Lin, Y., Huang, C., Irwin, D., He, L., Shang, Y., Yu, G., 2014. Three-dimensional flow contrast imaging of deep tissue using noncontact diffuse correlation tomography. Appl. Phys. Lett. 104, 121103.
Liu, J., Zhang, H., Lu, J., Ni, X., Shen, Z., 2017. Quantitative Model of Diffuse Speckle Contrast Analysis for Flow Measurement. SPIE, p. 11.
Maggio, P., Salinet, A.S., Robinson, T.G., Panerai, R.B., 2014. Influence of CO2 on neurovascular coupling: interaction with dynamic cerebral autoregulation and cerebrovascular reactivity. Phys. Rep. 2 e00280.
Mazdeyasna, S., Huang, C., Zhao, M., Agochukwu, N.B., Bahrani, A.A., Wong, L., Yu, G., 2018. Noncontact speckle contrast diffuse correlation tomography of blood flow distributions in tissues with arbitrary geometries. J. Biomed. Opt. 23, 096005.
Nowak, K., Mix, J., Gimsa, J., Strauss, U., Sriperumbudur, K.K., Benecke, R., Gimsa, U., 2011. Optimizing a rodent model of Parkinson's disease for exploring the effects and mechanisms of deep brain stimulation. Parkinsons Dis., 414682
O'Reilly, M.A., Muller, A., Hynynen, K., 2011. Ultrasound insertion loss of rat parietal bone appears to be proportional to animal mass at submegahertz frequencies. Ultrasound Med. Biol. 37, 1930–1937.
Reisman, M.D., Markow, Z.E., Bauer, A.Q., Culver, J.P., 2017. Structured illumination diffuse optical tomography for noninvasive functional neuroimaging in mice. Neurophotonics 4, 021102.
Schaller, B., Graf, R., 2002. Cerebral ischemic preconditioning - an experimental phenomenon or a clinical important entity of stroke prevention? J. Neurol. 249, 1503–1511.
Seevinck, P.R., Deddens, L.H., Dijkhuizen, R.M., 2010. Magnetic resonance imaging of brain angiogenesis after stroke. Angiogenesis 13, 101–111.
Seong, M., Phillips, Z., Mai, P.M., Yeo, C., Song, C., Lee, K., Kim, J.G., 2016. Simultaneous blood flow and blood oxygenation measurements using a combination of diffuse speckle contrast analysis and near-infrared spectroscopy. J. Biomed. Opt. 21, 27001.
Shang, Y., Chen, L., Toborek, M., Yu, G.Q., 2011. Diffuse optical monitoring of repeated cerebral ischemia in mice. Optic Express 19, 20301–20315.
Shang, Y., Zhao, Y., Cheng, R., Dong, L., Irwin, D., Yu, G., 2009. Portable optical tissue flow oximeter based on diffuse correlation spectroscopy. Optic Lett. 34, 3556–3558.
Sicard, K., Shen, Q., Brevard, M.E., Sullivan, R., Ferris, C.F., King, J.A., Duong, T.Q., 2003. Regional cerebral blood flow and BOLD responses in conscious and anesthetized rats under basal and hypercapnic conditions: implications for functional MRI studies. J. Cereb. Blood Flow Metab. 23, 472–481.
Stagliano, N.E., Perez-Pinzon, M.A., Moskowitz, M.A., Huang, P.L., 1999. Focal ischemic preconditioning induces rapid tolerance to middle cerebral artery occlusion in mice. J. Cereb. Blood Flow Metab. 19, 757–761.
Taber, K.H., Hillman, E.M., Hurley, R.A., 2010. Optical imaging: a new window to the adult brain. J. Neuropsychiatry Clin. Neurosci. 22 (iv), 357–360.
Takahashi, K., Greenberg, J.H., Jackson, P., Maclin, K., Zhang, J., 1997. Neuroprotective effects of inhibiting poly(ADP-ribose) synthetase on focal cerebral ischemia in rats. J. Cereb. Blood Flow Metab. 17, 1137–1142.
Teichert, M., Bolz, J., 2017. Simultaneous intrinsic signal imaging of auditory and visual cortex reveals profound effects of acute hearing loss on visual processing. Neuroimage 159, 459–472.
Tian, F., Liu, H., 2014. Depth-compensated diffuse optical tomography enhanced by general linear model analysis and an anatomical atlas of human head. Neuroimage 85 (Pt 1), 166–180.
Tian, F., Niu, H., Khadka, S., Lin, Z.J., Liu, H., 2010. Algorithmic depth compensation improves quantification and noise suppression in functional diffuse optical tomography. Biomed. Opt. Express 1, 441–452.
Ursino, M., Lodi, C.A., 1998. Interaction among autoregulation, CO2 reactivity, and intracranial pressure: a mathematical model. Am. J. Physiol. 274, H1715–H1728.
Valdes, C.P., Varma, H.M., Kristoffersen, A.K., Dragojevic, T., Culver, J.P., Durduran, T., 2014. Speckle contrast optical spectroscopy, a non-invasive, diffuse optical method for measuring microvascular blood flow in tissue. Biomed. Opt. Express 5, 2769–2784.
Varma, H.M., Valdes, C.P., Kristoffersen, A.K., Culver, J.P., Durduran, T., 2014. Speckle contrast optical tomography: a new method for deep tissue three-dimensional tomography of blood flow. Biomed. Opt. Express 5, 1275–1289.
Wagerle, L.C., Mishra, O.P., 1988. Mechanism of CO2 response in cerebral arteries of the newborn pig: role of phospholipase, cyclooxygenase, and lipoxygenase pathways. Circ. Res. 62, 1019–1026.
Wolk, R., Sieminska, J., Trzebski, A., 1995. Dual response of cerebrocortical blood flow and arterial blood pressure to transient CO2 stimulus after inhibition of nitric oxide synthesis in rats. Acta Neurobiol. Exp. 55, 73–84.
Wu, X., Eggebrecht, A.T., Ferradal, S.L., Culver, J.P., Dehghani, H., 2015. Fast and efficient image reconstruction for high density diffuse optical imaging of the human brain. Biomed. Opt. Express 6, 4567–4584.
Yu, G., Durduran, T., Furuya, D., Greenberg, J.H., Yodh, A.G., 2003. Frequency-domain multiplexing system for in vivo diffuse light measurements of rapid cerebral hemodynamics. Appl. Opt. 42, 2931–2939.
Yu, G., Lin, Y., Huang, C., 2018. Noncontact three-dimensional diffuse optical imaging of deep tissue blood flow distribution. US Patent 9,861,319.
Yuan, S., Devor, A., Boas, D.A., Dunn, A.K., 2005. Determination of optimal exposure time for imaging of blood flow changes with laser speckle contrast imaging. Appl. Opt. 44, 1823–1830.
Zhang, X., 2014. Instrumentation in diffuse optical imaging. Photonics 1, 9–32.
Zhou, C., Shimazu, T., Durduran, T., Luckl, J., Kimberg, D.Y., Yu, G., Chen, X.H., Detre, J.A., Yodh, A.G., Greenberg, J.H., 2008. Acute functional recovery of cerebral blood flow after forebrain ischemia in rat. J. Cereb. Blood Flow Metab. 28, 1275–1284.
Zhou, C., Yu, G., Furuya, D., Greenberg, J., Yodh, A., Durduran, T., 2006. Diffuse optical correlation tomography of cerebral blood flow during cortical spreading depression in rat brain. Optic Express 14, 1125–1144.
Zhou, Q., Wang, Y., Yi, L., Tan, Z., Jiang, Y., 2017. Multisensory interplay within human auditory cortex: new evidence from intraoperative optical imaging of intrinsic signal. World Neurosurg. 98, 251–257.